

# Unified Identification and Tuning Approach Using Deep Neural Networks For Visual Servoing Applications

Oussama Abdul Hay<sup>id</sup>, Mohamad Chehadeh<sup>id</sup>, *Member, IEEE*, Abdulla Ayyad<sup>id</sup>, *Member, IEEE*,  
Mohamad Wahbah<sup>id</sup>, Muhammad Humais<sup>id</sup>, and Yahya Zweiri<sup>id</sup>, *Member, IEEE*

**Abstract**—Vision based control of Unmanned Aerial Vehicles (UAVs) has been adopted by a wide range of applications due to the availability of low-cost on-board sensors and computers. Tuning such systems to work properly requires extensive domain specific experience which limits the growth of emerging applications. Moreover, obtaining performance limits of UAV based visual servoing with the current state-of-the-art is not possible due to the complexity of the models used. In this paper, we present a systematic approach for real-time identification and tuning of visual servoing systems based on a novel robustified version of the recent deep neural networks with the modified relay feedback test (DNN-MRFT) approach. The proposed robust DNN-MRFT algorithm can be used with a multitude of vision sensors and estimation algorithms despite the high levels of sensor's noise. Sensitivity of MRFT to perturbations is investigated and its effect on identification and tuning performance is analyzed. DNN-MRFT was able to detect performance changes due to the use of slower vision sensors, or due to the integration of accelerometer measurements. Experimental identification results were closely matching simulation results, which can be used to explain system behaviour and anticipate the closed loop performance limits given a certain hardware and software setup. Finally, we demonstrate the capability of the DNN-MRFT tuned visual servoing systems to reject external disturbances. Some advantages of the suggested robust identification approach compared to existing visual servoing design approaches are presented.

## I. INTRODUCTION

### A. Motivation

A variety of Unmanned Aerial Vehicles (UAVs) applications require visual servoing tasks as part of their overall mission. Many examples can be found in literature for such tasks like mission control [1], infrastructure inspection [2], and aerial manipulation [3]. From a broad perspective, visual servoing consists of three elements: vision sensor that provides a projection of the surrounding physical world, vision and state estimation algorithms that are used for data interpretation, and control algorithms that drive system states to desired references. Recent work on visual servoing for UAVs [4], [5] addressed the need for higher order dynamic models that describe UAVs' motion in order to achieve better control performance. Still these models are simplified in the sense

that the dynamics of the vision sensors, and vision and state estimation algorithms are absent. Although the authors in [4]–[6] presented system stability proofs, they did not present guarantees on system performance for a given set of controller parameters. Other researchers reported that addressing these parasitic dynamics is important to achieve optimal performance. For example, it is witnessed by [7] that the use of event cameras instead of vision cameras improved the dynamic performance of UAVs. Also, the work in [8] reported a significant change in the tracking performance of a moving visual target when the update rate of the visual detection is changed. The role of such parasitic dynamics in the tuning of high-performance systems is becoming widely acknowledged in the general robotics community. The effect of perception latency was studied in [9] for high speed sense and avoid applications. The value of latency was estimated using camera parameters. A drawback of this approach is that it requires careful analysis of the impact of the considered vision-based mission, as well as the used hardware and software setup on latency figures. Controller tuning becomes less systematic and heavily dependant on human-expert knowledge as a result of omitting such important parasitic dynamics, or as a result of handling it manually. All the visual servoing tasks presented in [10]–[12] used PID controllers with unclear strategy for controller parameters tuning. Tuning such controllers is not a straightforward task given the fact that the considered UAVs are underactuated where the interaction between the outer loops and the inner loops can be complex. In [13] the authors attempted to reduce this complexity by designing a non-linear controller with reduced number of tunable parameters, but servoing performance was poor. A main drawbacks of this approach is losing linear properties of the system which allow us to explain and predict system behaviour.

### B. Contributions

The contribution of this paper is to address systematic identification and tuning of UAV dynamics in a visual servoing setting in the presence of noisy sensor measurements. For this we utilize a novel robustified version of DNN-MRFT, which is a recently proposed identification and tuning approach based on Deep Neural Networks (DNN) and the Modified Relay Feedback Test (MRFT) [14]. In the presented approach, self-excited oscillations (limit cycles) are generated using MRFT, revealing distinct system features that are picked up by a DNN trained solely on simulation data. Emphasize of this work is given to handling noisy sensor measurements, and their effect on identification and tuning performance. Predictability

This work was supported by Khalifa University grants CIRA-2020-082 and RC1-2018-KUCARS. Oussama Abdul Hay is the corresponding author (email: [oussama.hay@ku.ac.ae](mailto:oussama.hay@ku.ac.ae)).

O. Abdul Hay, M. Chehadeh, A. Ayyad, M. Wahbah, M. Humais, and Y. Zweiri are with the Center for Autonomous Robotic Systems, Khalifa University, Abu Dhabi, United Arab Emirates. Y. Zweiri is also with the Faculty of Science, Engineering and Computing, Kingston University London, London, SW15 3DW, UK.

\*Oussama Abdul Hay and Mohamad Chehadeh contributed equally to this work.

of system performance is presented by demonstrating the match between simulated identified models' responses and experimental responses. The effect of the use of different sensors, and sensor fusion structures on the performance of system dynamics is demonstrated using a single unifying framework. The sensors used are a camera (i.e. frame-based visible wavelength camera, will be referred to as normal or RGB camera), an event based camera (also known as dynamic vision sensor, will be referred to as event camera), and a thermal camera. DNN-MRFT is a lightweight algorithm that can be used for real-time identification and tuning. To the best of our knowledge, this is the first reporting in literature for a real-time identification and tuning method applied to UAVs that use on-board sensors for control. As a result of the proposed novel approach, our UAV achieves near optimal step reference following performance despite being tuned in real-time and without requiring any additional manual tuning. The demonstrated optimality is against the integral square error (ISE) metric, which is a representative of the whole frequency spectrum. The tuned system was able to withstand wind disturbances as high as 3.5m/s, and external pull and release disturbance with forces up to 10N.

### C. Scope

It is important to highlight that the proposed contribution is applicable to a wide variety of UAV visual servoing tasks, including image based visual servoing (IBVS) and position based visual servoing (PBVS). Without loss of generality, the proposed approach will be demonstrated in this paper by commanding the UAV to lock and move relative to a target that is fixed to a planar vertical structure. In another case, the target moves arbitrarily in discrete large steps and the UAV needs to keep following the target. Such step changes are not uncommon in visual servoing scenarios, e.g. recovery from occlusions or temporal out of field of view state. In all cases, the distance to target is assumed to be known, thus we consider a PBVS scenario. This arrangement was inspired by Challenge 3 of Mohamed Bin Zayed International Robotics Challenge 2020 (MBZIRC2020) [15] where firefighting UAVs were used to target fires both indoors and outdoors. Intuitively, same techniques presented in this paper can be applied to other arrangements like servoing an object on the ground. Tuning controllers to follow other trajectories can be considered as an extension to this work where optimality with regards to excitation sources other than a step could be used.

## II. STATE ESTIMATION

The main system components of the visual servoing design suggested in this paper is outlined in Fig. 2. The proposed system might be operating in one of these two phases: identification phase or control phase. In this section we discuss various aspects of state estimation, and in the next section we discuss modeling and identification through DNN-MRFT.

In this work, we define the inertial frame  $\mathcal{F}_I$  to be earth-fixed reference frame with  $i_z$  basis pointing upwards. The body reference frame  $\mathcal{F}_B$  is attached to the multirotor UAV

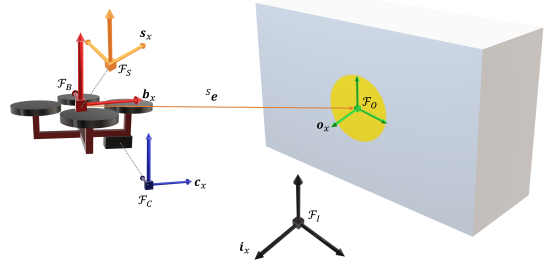


Fig. 1: Illustration of the reference frames used in this paper. Note that the camera and IMU reference frames are offsetted for visual clarity.

center of mass, with  $b_z$  perpendicular to the propulsion plane, and is pointing in the thrust direction. Another body attached reference frame is the camera reference frame  $\mathcal{F}_C$  with  $c_x$  basis aligned with the focal vector of the camera and centered at the sensor center. For convenience, we define another reference frame  $\mathcal{F}_O$  that is attached to the tracked object with  $o_x$  basis always perpendicular to the object plane. The last used reference frame is the servoing reference frame  $\mathcal{F}_S$  with its origin coinciding with  $\mathcal{F}_B$  origin, and with basis definition  $s_x = -o_x$ . The servoing error is then defined as (note that all vectors are in  $\mathcal{F}_S$ ):

$$s_e = {}^S r_c - s_c \quad (1)$$

where  ${}^S c$ , and  ${}^S r_c$  are the object center and desired reference respectively (all in meters). Note that the error is negated here, compared to the convention widely used in visual servoing literature [16]. Fig. 1 provides a graphical illustration of the utilized reference frames and the error vector. All the reference frames are right-handed and a counter clockwise rotation is positive by definition. A pose transformation defined in  $SE(3)$  Lie group used to transform between reference frames is denoted by  ${}^B_A T$ , where  $B$  is the target reference frame and  $A$  is the source one, and where  $T$  is a 4 by 4 matrix with unity homogeneous coordinates.

### A. Object Detection and Position Estimation

The object detection task is greatly simplified in our case due to the prior knowledge of the object shape. During visual servoing, the UAV position is referenced to the center of the detected object. We have used a screen projector to project shapes on the wall. With this setup, we can easily create different object shapes and program their motion. For the normal and event cameras, the task was to track a circle. The detection pipeline included a blob detector to retrieve the circle's center  $o = [o_x \ o_y]^T$  in pixel coordinates. For the event camera, we use a checkered circle that is rotating at a fixed speed to ensure continuous generation of events. Still the generated events do not fully form a circle, and a connected set algorithm is used to form a circle. We used a rectangular thermal source to be detected by the thermal camera, where a simple threshold is applied to mask the thermal source.

Changes to the detected shape has no effect on the followed methodology.

To recover relative position from detected object center, we use the pinhole camera model given by [16]:

$$\begin{cases} p_y = \frac{c_y}{c_x} = \frac{o_x - c_u}{f\alpha} \\ p_z = \frac{c_z}{c_x} = \frac{o_y - c_v}{f} \end{cases} \quad (2)$$

where  ${}^C\mathbf{p} = [f p_y p_z]^T$  is the projected center on the image plane,  ${}^C\mathbf{c} = [c_x c_y c_z]^T$  is the center of the detected object in  $\mathcal{F}_C$ , and  $c_u, c_v, f, \alpha$  are the pre-known intrinsic camera parameters. The observation  $\mathbf{p}$  can be transformed to the  $\mathcal{F}_S$  frame by utilizing knowledge of the object plane direction, and the heading of the UAV. Such transformation would allow us to incorporate depth measurements, which are reported in  $\mathcal{F}_S$ . This can be achieved by using:

$${}^S\mathbf{c} = {}^S d ({}^S_B T_C^B T^C \mathbf{p}) \quad (3)$$

where  ${}^S d$  is a depth measurement projected on  $s_x$  basis. Once Eq. (3) is evaluated and  $r_c$  is chosen, the error vector in Eq. (1) is known and we can design a controller to minimize it.

### B. Sensors Setup and Calibration

For both the normal camera (we used Intel D435i updating at 60Hz) and the event camera (we used iniVation DVS346 updating at 100Hz) we performed intrinsic camera parameters calibration using a checker board. The IMU we used is Xsens MTi-670 and is updating at 200Hz where we also calibrate for gyro drift prior to every flight. We assume a simplified accelerometer error model, and we use position measurements to calibrate accelerometer bias during hover, assuming uncorrelated 3-axis measurements. The static transformation  ${}^B_C T$  was found using a CAD model. We found temporal calibration between the IMU and the camera measurements to be the most important. Without temporal synchronization, errors as large as 0.5m were observed when servoing at around 4m distance from the object. ROS package *messagefilter* was used for the temporal synchronization of sensors' measurements.

### C. Design of Kalman Filter

We used a Kalman Filter (KF) to obtain smoother and higher rate  ${}^S\mathbf{e}$  and  ${}^S\dot{\mathbf{e}}$  estimates. A decoupled kinematic model was used to design the filter, which separates the rotational and linear motion estimates. The decoupling allows the design of three independent KF's, one along each inertial axis. The filtered states for a single KF are the position  $p$ , velocity  $v$ , and an estimate of the acceleration bias  $a_b$  which was added to adjust for gravity. The prediction model used is:

$$\mathbf{x}_{k+1} = \begin{bmatrix} p_{k+1} \\ v_{k+1} \\ a_{b,k+1} \end{bmatrix} = \begin{bmatrix} 1 & \Delta t & -\Delta t^2 \\ 0 & 1 & -\Delta t \\ 0 & 0 & 1 \end{bmatrix} \mathbf{x}_k + \begin{bmatrix} \Delta t^2 \\ \Delta t \\ 0 \end{bmatrix} u_k + \mathcal{N}(0, \sigma_p) \quad (4)$$

where  $\mathbf{x}$  is the state vector, the subscript  $k$  is an integer multiple of the step time  $\Delta t$ ,  $u$  is the control signal, and  $\mathcal{N}(0, \sigma_p)$  is a zero mean normally distributed additive noise

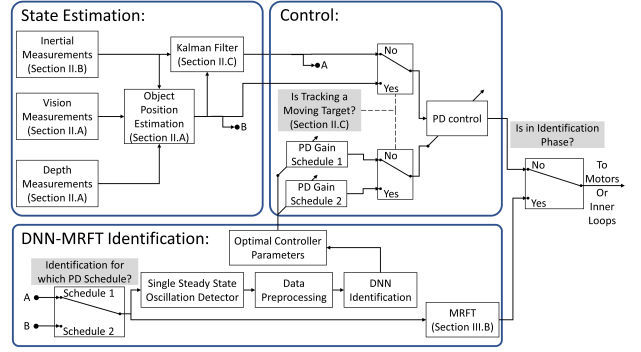


Fig. 2: Overall identification structure for visual servoing. Controller Schedule 1 is used for the case when a KF is used to fuse IMU measurements and vision measurements. Controller Schedule 2 is used when vision based measurements are used without being fused with the IMU measurements.

with variance  $\sigma_p$ . The control signal is obtained from rotating the accelerometer measurement into the inertial frame. The aforementioned model assumes an exact knowledge of the rotation of the UAV, and an identical additive noise profile of the three accelerometer axes, such that  $u$  is not scaled improperly due to misalignment, and  $\sigma_p$  doesn't change as the UAV rotates. The correction step uses the position estimate from the camera, described in section II-A, with the addition of measurement noise  $\mathcal{N}(0, \sigma_c)$ . The KF cannot be used when the tracked object starts moving as such movements are not captured by the inertial sensors thus introducing inconsistency in the filter states. Consequently, the KF can be only used when the object is stationary, and when it moves we have to solely depend on camera measurements. This is reflected in the state estimation part of Fig. 2 where a large error in the Kalman prediction step triggers the change of the controller schedule. The state estimator linearized dynamics will be picked up in the identification phase, and hence more sophisticated nonlinear estimators like those suggested in [17], [18] can still be used in this approach. Furthermore, a recent approach which uses the DNN-MRFT to design a dynamic based KF can be used to provide state estimates at higher rates [19].

### III. IDENTIFICATION AND CONTROLLER TUNING

DNN-MRFT was suggested in [14] as a real-time system identification method. Using DNN-MRFT, the authors in [20] demonstrated unprecedented identification and tuning capability where a multirotor UAV could take-off without a prior knowledge of its own dynamics and achieve aggressive trajectory tracking within a few seconds of identification. In this work we extend the application of DNN-MRFT to visual servoing for multirotor UAVs. As outlined in Fig. 2, for each of the altitude and lateral motion loops we identify two systems: one with the Kalman filter and another one without it (i.e. just relying on camera measurements). The Kalman filter provides better dynamic response of the closed loop system, but it cannot be used for the case when the tracked target is

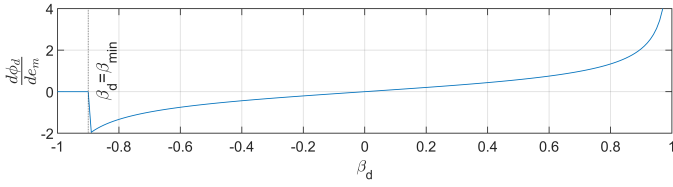


Fig. 3: Sensitivity of test phase as a result of perturbations on  $e_m$ . The test phase is insensitive to such perturbations when  $\beta_d < \beta_{min}$  due to the nonlinear filter in Eq. (12). These sensitivity results assumes nominal value of  $\bar{e}_m = 1$ .

moving arbitrarily. DNN-MRFT regards system identification as a classification problem and uses a deep neural network solely trained on simulation data, and hence the structure of the model needs to adequately capture the system behaviour. Vision based perception systems usually suffer from high level of noise, and for that a robust version of DNN-MRFT is necessary to develop, and its effect on identification accuracy and tuning performance need to be investigated.

#### A. Selection of Dynamic Model

A multirotor UAV is a rigid body in  $\mathbb{R}^3$ , having 6 degrees-of-freedom (DOF) and subject to forces and torques in  $\mathbb{R}^3$ . It is assumed that the multirotor UAV CoG is coincident with the IMU center, intersects the propellers plane, and is also coincident with the body frame  ${}^B\mathcal{F}$  origin. Also we assume the UAV body to be symmetric around all axes. Forces and torques are applied to the rigid body by the actuators, where they are assumed to be mapped from the electronic speed controllers (ESCs) inputs by the following linear propulsion system dynamics:

$$G_{prop}(s) = \frac{K_{eq}e^{-\tau s}}{T_{prop}s + 1} \quad (5)$$

where  $K_{eq}$ ,  $\tau$ , and  $T_{prop}$  are lumped parameters describing overall dynamics [21]. Following the modeling approach detailed in [20], [22] we linearize the nonlinear dynamics of multirotors around the hover state, and cascade the actuator dynamics to obtain the following attitude and altitude dynamics:

$$G_{inner}(s) = \frac{K_{eq}e^{-\tau_{in}s}}{s(T_{prop}s + 1)(T_1s + 1)} \quad (6)$$

and the lateral motion dynamics are given by:

$$G_{lat}(s) = \frac{K_{eq}e^{-\tau_{out}s}}{s^2(T_{prop}s + 1)(T_1s + 1)(T_2s + 1)}, \quad (7)$$

The overall lumped dynamics presented in Eqs. (6) and (7) account for sensor dynamics. Sensor dynamics are mainly exhibited by a time delay, and therefore would be picked up by the identification algorithm.

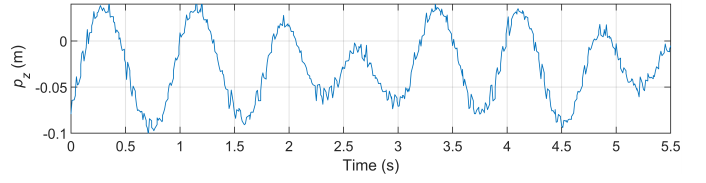


Fig. 4: Variations in oscillations' amplitudes due to temporal variations in test phases for the case of event camera based servoing without KF. The temporal variations in test phases are due to perturbations in the value of  $e_m$ . Note that the filter introduced in Eq. (12) prevented false switching that might occur due to the local peaks and anti-peaks introduced to the main periodic signal by noise.

#### B. Robust MRFT

The input to the DNN is a limit cycle generated by MRFT, which is a relay controller realized by the following algorithm:

$$u_M(t) = \begin{cases} h & : e(t) \geq b_1 \vee (e(t) > -b_2 \wedge u_M(t-) = h) \\ -h & : e(t) \leq -b_2 \vee (e(t) < b_1 \wedge u_M(t-) = -h) \end{cases} \quad (8)$$

where  $b_1 = -\beta e_{min}$  and  $b_2 = \beta e_{max}$ ,  $e_{max} > 0$  and  $e_{min} < 0$  are the last maximum and minimum values of the error signal after crossing the zero level respectively, and  $u_M(t-) = \lim_{\epsilon \rightarrow 0^+} u_M(t - \epsilon)$  is the last control output. Initially we set  $e_{max} = e_{min} = 0$ .  $\beta$  is a tunable parameter that defines the phase of the excited oscillations and is bound by  $-1 < \beta < 1$ . Using the describing function (DF) method we could shown that the self-excited oscillations satisfy the HB equation [23]:

$$N_d(a_0)G(j\Omega_0) = -1 \quad (9)$$

The DF of MRFT is presented in [24] as:

$$N_d(a_0) = \frac{4h}{\pi a_0} (\sqrt{1 - \beta^2} - j\beta) \quad (10)$$

Details on obtaining the optimal value of  $\beta$  are provided in [20], which in our case was found to be  $\beta_{z0} = -0.72$  for the altitude loop, and for lateral control loop the optimal value  $\beta_{x0}$  changes based on the identified attitude loop dynamics. It is also shown in [20] that the periodic motions for the considered multirotor UAV dynamics are stable. Stability is still guaranteed for the case of visual servoing where we could potentially have higher delays in the system. Due to the use of a nonlinear DNN, inaccuracies due to the sinusoidal assumption of the error signal can be relaxed, and the DNN could provide the inverse map of an arbitrary shape of the periodic error signal. The shape of the error signal depends on the relative degree and the time delays present in the underlying system [25]. Indeed, the MRFT algorithm given in Eq. (8) does assume a sinusoidal error signal and provide a switching phase based on the detected extrema in the error signal  $e_{max}$  or  $e_{min}$ . Apparently perturbations on the extrema values due to the use of noisy vision sensors would cause errors in switching phases.

Stability of the periodic oscillations for the considered model structure was shown in [20], which suggests that the effect of such perturbations would be eventually damped. In a more sever case the false detection of local extrema would result in arbitrary fast switching causing oscillations that capture noise dynamics, not the unknown system dynamics. Consider the following zero-mean noise model:

$$e(t) = \bar{e}_m \sin \Omega_0 t + k_1 \sin \Omega_n t + \psi_n + k_2 w_n(t) \quad (11)$$

where  $\bar{e}_m \in \{e_{max}, e_{min}\}$  is the extrema of the true signal,  $k_1, k_2 \ll \bar{e}_m$ ,  $\Omega_n$  is the frequency of the slowest periodic noise where  $\Omega_n \gg \Omega_0$ , and  $w_n(t)$  is a zero-mean high frequency noise signal with maximum amplitude of  $k_2$ . The periodic component  $k_1 \sin \Omega_n t + \psi_n$  represents unwanted signals due to high frequency attitude oscillations. As the switching might occur due to local extrema caused by  $k_1 \sin \Omega_n t + \psi_n$ , we design the following peak detection condition:

$$e_m[n] = \begin{cases} e_m(t - T_n) : \sup\{\pm e(t) | t \in [t - \tau_n, t]\} = e(t - T_n) \\ 0 : \sup\{\pm e(t) | t \in [t - T_n, t]\} \neq (t - T_n) \wedge e_m[n] = 0 \end{cases} \quad (12)$$

where the index  $n$  indicates the extrema of the current period, the  $\pm$  accounts for the fact that anti-peak needs to be detected as well, and  $T_n = \frac{2\pi}{\Omega_n}$ . This peak detection condition introduces lag to the  $e_m$  detection process. As a result, the minimum value of  $\beta$  that is realizable would be limited to  $\beta_{min} = -1 + \sin \frac{T_n}{T_0} 2\pi$ . The values of  $T_n$  and  $T_0$  are obtained experimentally, and are specific for every sensor used (e.g. for normal camera with KF,  $\frac{T_n}{T_0} = 0.015$  which results in  $\beta_{min} = -0.906$ ).  $\beta_{min}$  for most cases was smaller than  $\beta_{z0}$  which allowed us to realize the optimal value of the phase of the test. In the case of thermal camera when KF was not used, realizing stable oscillations at  $\beta_{z0}$  was not possible, and hence the value of  $\beta_{z0}$  was shifted from the optimal test phase.

As a result of the added noise, a deviation in  $e_m$  will be introduced which we model by:

$$e_m = \bar{e}_m + k\delta(t) \quad (13)$$

where  $\delta(t)$  is the Dirac function and  $k$  is a random variable with  $k \in [-(k_1 + k_2), k_1 + k_2]$ . Assuming a desired switching phase  $\beta_d = \sin \phi_d$ , then the relation between the switching phase and the extrema values is given by:

$$\phi_d = \arcsin(\beta_d \frac{e_m}{\bar{e}_m}) \quad (14)$$

And the sensitivity of the switching phase to the changes in  $e_m$  is given by:

$$\frac{d\phi_d}{de_m} = \frac{\beta_d}{\bar{e}_m} \frac{1}{\sqrt{1 - (\frac{\beta_d e_m}{\bar{e}_m})^2}} \quad (15)$$

The sensitivity of the system for small amplitude perturbations, i.e.  $e_m \approx \bar{e}_m$ , for different  $\beta_d$  values are shown in Fig. 3. Note that for the case of the conventional RFT [26] when  $\beta_d = 0$  the system is insensitive to extrema perturbations. The system

becomes more sensitive to such perturbations as  $|\beta_d|$  increases except for when  $\beta_d < \beta_{min}$ . As a result of the temporal change in test phase due to these perturbations and due to the fact that periodic oscillations are stable, the amplitude of the periodic oscillations *swings* around  $\bar{e}_m$ . This becomes clear when noisy sensors are used as in the case of event camera as can be seen in Fig. 4. The amplitude swings due to the phase swing is related in a nonlinear way and can be characterized by the change in the system amplitude response, to the system phase response. For example, this relation for the attitude and altitude loops model given in Eq. (6) is:

$$\frac{d|G_{inner}|}{d\angle G_{inner}} = \frac{\frac{d|G_{inner}|}{d\Omega}}{\frac{d\angle G_{inner}}{d\Omega}} = \frac{K_{eq}(-\frac{1}{\Omega^2}C_1 - \frac{T_{prop}^2\Omega}{(\Omega^2 T_{prop}^2 + 1)^{\frac{3}{2}}}C_2 - \frac{T_1^2\Omega}{(\Omega^2 T_1^2 + 1)^{\frac{3}{2}}}C_3)}{\frac{-T_{prop}}{\sqrt{1 - (T_{prop}\Omega)^2}} - \frac{T_1}{\sqrt{1 - (T_1\Omega)^2}} - \tau_{in}} \quad (16)$$

where  $C_1 = (\Omega^2 T_{prop}^2 + 1)^{-\frac{1}{2}} (\Omega^2 T_1^2 + 1)^{-\frac{1}{2}}$ ,  $C_2 = \Omega^{-1} (\Omega^2 T_1^2 + 1)^{-\frac{1}{2}}$ ,  $C_3 = \Omega^{-1} (\Omega^2 T_{prop}^2 + 1)^{-\frac{1}{2}}$ . The term  $d|G_{inner}|/d\angle G_{inner}$  is non-singular for  $\Omega > 0$  as the system is minimum phase. We performed a numerical analysis to verify the accuracy of averaging of oscillations around  $\Omega_0$  based on the identification values obtained experimentally and based on the relation given in Eq. (16). We estimated the error in gain to be less than 0.1% off the true value for the worst case, which can be obviously neglected. Similar results can be obtained for the lateral motion dynamics described by Eq. (7).

### C. Identification with DNN-MRFT

Using a classification approach for identification provides several advantages like the computational efficiency in training, and the ability to provide optimal controller parameters in a lookup table for real-time tuning. Controller parameters are tuned to minimize the ISE cost for a step reference. It is possible with DNN-MRFT to obtain, for the same system, two different sets of the lumped system parameters that would result in the same (or very similar) tuning controller parameters and hence the same closed loop system performance. This is because DNN-MRFT benchmarks identification accuracy based on the closed loop system performance. In DNN-MRFT the relative sensitivity function is used as a distance measure in the system parameters' space and is given by [27]:

$$J_{ij} = \frac{Q(C_i, G_j) - Q(C_j, G_j)}{Q(C_j, G_j)} \times 100\% \quad (17)$$

where  $J_{ij}$  represents the degradation in performance due to applying controller  $C_i$ , which is the optimal controller for the process  $G_i$  and a sub-optimal controller for the process  $G_j$ .  $Q$  is a function that calculates the ISE of the step response of the closed loop system. Note that  $J_{ij} \neq J_{ji}$  so we define  $J_{(ij)} = \max(J_{ij}, J_{ji})$ . This fact is utilized by the DNN

TABLE I: Identification and tuning results with a normalized step ISE cost comparison between simulation and experimentation - altitude control loop.

Sensor	$T_{prop}$	$T_1$	$\tau_{in}$	$K_p$	$K_d$	$Q_{exp}$	$Q_{sim}$	
with KF	Normal	0.30	0.20	0.0128	1.1766	0.3143	0.0874	0.080
	Event	0.30	0.20	0.0128	1.2993	0.3471	0.0771	0.0698
	Thermal	0.1675	0.6523	0.0048	1.7766	0.5352	0.0933	0.0684
without KF	Normal	0.1355	1.6825	0.06	0.3739	0.1705	0.2174	0.1629
	Event	0.0135	1.6834	0.0237	0.888	0.3258	0.1293	0.1068
	Thermal	0.2766	2.0059	0.0022	0.257	0.1435	-	-

TABLE II: Identification and tuning results with a normalized step ISE cost comparison between simulation and experimentation - lateral motion control loop.

Sensor	$T_2$	$\tau_{out}$	$K_p$	$K_d$	$Q_{exp}$	$Q_{sim}$	
with KF	Normal	0.40	0.0825	1.4343	0.5662	0.2608	0.2574
	Event	3.6789	0.01	1.0155	0.5270	0.3332	0.2556
	Thermal	0.40	0.30	0.9089	0.4962	0.2523	0.3580
without KF	Normal	3.6789	0.01	0.9403	0.488	0.3855	0.3449
	Event	3.6789	0.01	0.8154	0.4231	0.2479	0.1927
	Thermal	0.40	0.30	0.3585	0.1957	-	-

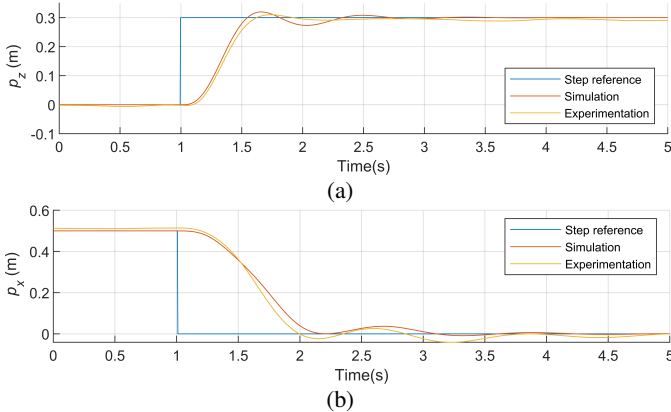


Fig. 5: System response to a step reference change when normal camera was used with a KF to estimate position and velocity. PD parameters used correspond to Schedule 1 in Fig. 2.

modified softmax function with cross-entropy loss introduced in [14]:

$$p_i = \frac{e^{J_{il} \cdot a_i}}{\sum_{j=1}^N e^{J_{jl} \cdot a_j}} \quad (18)$$

where  $l$  represents the label index available in the training and:

$$\frac{\partial L}{\partial a_i} = J_{il} \times (p_i - y_i) \quad (19)$$

is the backpropagation term for the one-hot encoded vector. The involvement of the  $J_{il}$  in training the network caused the DNN to avoid misclassifications that would result in significant performance drop or instability. The DNN structure selected consists of two hidden layers with ReLU activation functions, and ADAM optimizer was used. To avoid overfitting, the training data is augmented with white Gaussian noise and random bias is introduced to the dynamical system.

#### IV. RESULTS

For all experiments, we have used a hexarotor UAV running on a custom flight controller software. The main loop runs on

a Raspberry PI 3B embedded computer with the NAVIO2 extension board. The main control loop runs at 200Hz in a ROS node. Without the camera payload, the hexarotor dimensions are  $111 \times 100 \times 27$ cm, it weighs 3.38kg, and has the estimated rotational inertia of  $J_x = 0.093$ ,  $J_y = 0.089$ ,  $J_z = 0.156$  all in  $kg \cdot m^2$ . We have used E600 propulsion system from DJI, which accepts a PWM command with a pulse width in the range of 1ms to 2ms. We measured on a bench test the saturation values of the propulsion system and found them to be at  $1165\mu s$  and  $1878\mu s$ . Additionally, a saturation value of  $\pm 0.2617 rad$  were applied to the controller output of the lateral motion control loop. Also we have added a Butterworth second order low-pass filter with a cutoff frequency of 20Hz. All the saturation values and filters used in experimentation are reflected in all our simulations. The experimental results are summarized in the supplementary video which can be also found in [28].

#### A. Identification Results

System identification is performed twelve times in total: twice for every control schedule (refer to Fig. 2) for every sensor used over two control loops. These results can be found in Table I for the altitude control loop, and in Table II for the lateral motion control loop. Following the homogeneous tuning approach presented in [24], we have constrained the minimum phase margin to be  $20^\circ$  for all the tuning cases. We have used PD controllers for all control loops. The PD controller of the lateral motion outer loop provides the set-point for the corresponding inner loop attitude loop.

The results in Tables I and II show that for the case when the KF is used most sensors resulted in a similar controller parameters. The closed loop performance for altitude and lateral step tracking is similar for all cameras used despite the difference in the sensor dynamics. This is explained by the fact that the IMU dynamics in the KF dominate for the range of frequencies used for identification. The results in Tables I and II also show the match between step costs obtained in simulation and experimentation. Note that finding the step cost for the case when the tracked target moves in a step requires some approximations as the target movement is not

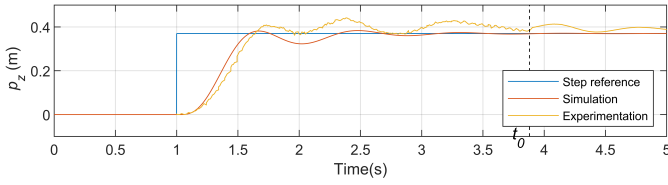


Fig. 6: System response to a step change in object altitude when an event camera was solely used to estimate position and velocity. PD parameters used correspond to Schedule 2 shown in Fig. 2. The switch back to the PD Schedule 1 happens at the moment indicated by the vertical dashed line when the system reaches a steady state condition.

synced with the on-board measurements. Fig. 5 shows the step response match between simulations and experimentation for the case of normal camera. The qualitative behaviour (i.e. overshoot, oscillations nature and decay characteristics, etc.) shown in experimentation matches the simulated system. This is an evidence of the correctness of the used model structure. From a quantitative perspective, the percentage overshoot (PO) of the simulated system for the normal camera case with KF on altitude step is 6.32% which is quite comparable with 7.85% obtained experimentally. The error in rise time  $T_r$  between simulation and experimentation was 13.4% for the same step case. The error figures were smallest for the normal camera as it has highest resolution and lowest noise. Overall, these small error figures combined with low variance in identification results, prove that online identification approach based on DNN-MRFT can be used to accurately perform identification and tuning in real-time for visual servoing tasks.

### B. Disturbance Rejection

We have performed a few disturbance rejection tests. The disturbance types we have considered are tracked target step changes (i.e. vision disturbance), wind disturbances, and pull and release disturbance. Tracking a step change of a target requires the use of control parameters schedule tuned without the KF. Step following is the extreme case of vision target tracking as a step is not Lipschitz and methods similar to those proposed in [6], [29] for approximating the target motion model would not work under the assumption that the tracked target might move arbitrarily. The identification without the KF showed significant drop in the system gains for the altitude loops compared to the case when the identification is done with the KF due to higher observed lag in the system as reported in Table I. The system  $T_r$  for the altitude control loop increased from 0.63 to 0.71 for the normal camera, and from 0.49 to 0.64 for the event camera when the KF was not used. Table I shows a better step tracking performance with event camera on the altitude loop. In experimentation, the normal camera resulted in a 67% worse ISE performance compared with the event camera. This is expected due to the high update rate and lower latency of the event camera which agrees with the results reported in [9]. On the other hand, it is interesting to observe a slight drop in the controller performance for the

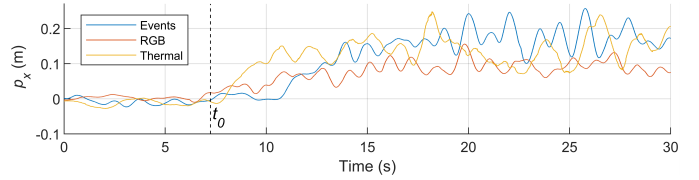


Fig. 7: Response of multirotor for every type of vision sensor used for an external wind disturbance with wind speed of 3.5m/s. The fan was turned on at time  $t_0$ .

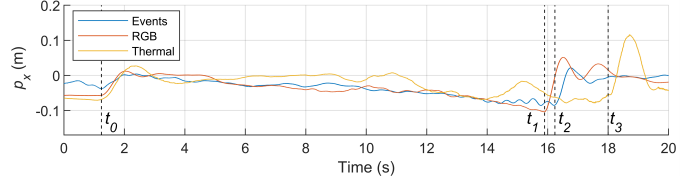


Fig. 8: Response of multirotor for every type of vision sensor used for a pull force of 10N followed by an instantaneous release. The thread pull starts at time  $t_0$  and the thread cut happened at  $t_1$  for the normal camera, at  $t_2$  for the event camera, and at  $t_3$  for the thermal camera case.

lateral motion control loop case (refer to Table II) when the KF is not used. This is due to the fact that the faster inner loop dynamics, which use on-board IMU measurements, are dominant in the lateral motion control loop. Fig. 6 shows the response of a UAV with event camera to a step change in the location of the tracked object. We could not run the tracked target step change experiment with the thermal camera due to the large noise resulted from position differentiation.

A steady-state error is expected for the case of wind disturbances when PD controllers are used. Fig. 7 shows the wind disturbance rejection performance where a wind speed of around 3.5m/s is applied to the hovering multirotor UAV with the three different sensors. The platform reacts adequately to the disturbance and deviates by less than 18cm from the hover position for the normal camera case. The platform deviated more from the hover position for the other two sensors due to the lower  $K_p$  values of the controller, which is expected.

Pull and release disturbance alters system dynamics in the pull phase as the UAV becomes linked with the human body. At the release instant the system would have an initial states condition that needs to be driven to the equilibrium point again. The pull and release disturbance is similar in nature to the case of recovery from collisions or random initial flight condition. We tested the system with all vision sensors by applying a force of 10N in the pull phase then releasing the system by cutting the pull thread. Fig. 8 shows the system response to a pull and release disturbance for all the used cameras.

## V. CONCLUSIONS

A systematic approach for system identification and controller tuning based on DNN-MRFT for visual servoing was

presented. The suggested approach provided several advantages over existing approaches in the visual servoing literature such as the real-time identification capability, the ability to account for delay dynamics, and the systematic tuning. The suggested approach was tested on a multitude of sensor and estimator configurations that are common in visual servoing tasks with UAVs. The demonstrated match between experimentation and simulation can be used to predict the system behaviour for different tuning settings and changes in system parameters. The presented automatically tuned closed loop system demonstrated adequate and stable performance against different external disturbances. In future work we aim at investigating the application of the presented approach for tracking of targets having a continuous movement at high speeds, and to further analyse performance mismatch when performing identification with slow update rate sensors.

## REFERENCES

- [1] J. Thomas, G. Loianno, K. Daniilidis, and V. Kumar, "Visual servoing of quadrotors for perching by hanging from cylindrical objects," *IEEE Robotics and Automation Letters*, vol. 1, no. 1, pp. 57–64, 2016.
- [2] K. Máthé and L. Búsoniu, "Vision and control for uavs: A survey of general methods and of inexpensive platforms for infrastructure inspection," *Sensors*, vol. 15, no. 7, pp. 14 887–14 916, 2015. [Online]. Available: <https://www.mdpi.com/1424-8220/15/7/14887>
- [3] H. Bonyan Khamseh, F. Janabi-Sharifi, and A. Abdessameud, "Aerial manipulation—a literature survey," *Robotics and Autonomous Systems*, vol. 107, pp. 221 – 235, 2018. [Online]. Available: <http://www.sciencedirect.com/science/article/pii/S0921889017305535>
- [4] V. Lippiello, J. Cacace, A. Santamaria-Navarro, J. Andrade-Cetto, M. A. Trujillo, Y. R. R. Esteves, and A. Viguria, "Hybrid visual servoing with hierarchical task composition for aerial manipulation," *IEEE Robotics and Automation Letters*, vol. 1, no. 1, pp. 259–266, 2015.
- [5] J. Thomas, G. Loianno, K. Daniilidis, and V. Kumar, "Visual servoing of quadrotors for perching by hanging from cylindrical objects," *IEEE robotics and automation letters*, vol. 1, no. 1, pp. 57–64, 2015.
- [6] J. Thomas, J. Welde, G. Loianno, K. Daniilidis, and V. Kumar, "Autonomous flight for detection, localization, and tracking of moving targets with a small quadrotor," *IEEE Robotics and Automation Letters*, vol. 2, no. 3, pp. 1762–1769, 2017.
- [7] E. Mueggler, B. Huber, and D. Scaramuzza, "Event-based, 6-dof pose tracking for high-speed maneuvers," in *2014 IEEE/RSJ International Conference on Intelligent Robots and Systems*. IEEE, 2014, pp. 2761–2768.
- [8] H.-M. Chuang, D. He, and A. Namiki, "Autonomous target tracking of uav using high-speed visual feedback," *Applied Sciences*, vol. 9, no. 21, 2019. [Online]. Available: <https://www.mdpi.com/2076-3417/9/21/4552>
- [9] D. Falanga, S. Kim, and D. Scaramuzza, "How fast is too fast? the role of perception latency in high-speed sense and avoid," *IEEE Robotics and Automation Letters*, vol. 4, no. 2, pp. 1884–1891, 2019.
- [10] T. Oliveira and P. Encarnação, "Ground target tracking control system for unmanned aerial vehicles," *Journal of Intelligent & Robotic Systems*, vol. 69, no. 1, pp. 373–387, 2013.
- [11] A. Borowczyk, D.-T. Nguyen, A. Phu-Van Nguyen, D. Q. Nguyen, D. Saussié, and J. Le Ny, "Autonomous landing of a multirotor micro air vehicle on a high velocity ground vehicle," *Ifac-Papersonline*, vol. 50, no. 1, pp. 10 488–10 494, 2017.
- [12] L. Zhang, F. Deng, J. Chen, Y. Bi, S. K. Phang, X. Chen, and B. M. Chen, "Vision-based target three-dimensional geolocation using unmanned aerial vehicles," *IEEE Transactions on Industrial Electronics*, vol. 65, no. 10, pp. 8052–8061, 2018.
- [13] H. Cheng, L. Lin, Z. Zheng, Y. Guan, and Z. Liu, "An autonomous vision-based target tracking system for rotorcraft unmanned aerial vehicles," in *2017 IEEE/RSJ International Conference on Intelligent Robots and Systems (IROS)*. IEEE, 2017, pp. 1732–1738.
- [14] A. Ayyad, M. Chehadeh, M. I. Awad, and Y. Zweiri, "Real-time system identification using deep learning for linear processes with application to unmanned aerial vehicles," *IEEE Access*, vol. 8, pp. 122 539–122 553, 2020.
- [15] "The mohamed bin zayed international robotics challenge 2020." [Online]. Available: <https://www.mbzirc.com/challenge/2020>
- [16] F. Chaumette, S. Hutchinson, and P. Corke, "Visual servoing," in *Springer Handbook of Robotics*. Springer, 2016, pp. 841–866.
- [17] M. K. Al-Sharman, B. J. Emran, M. A. Jaradat, H. Najjaran, R. Al-Husari, and Y. Zweiri, "Precision landing using an adaptive fuzzy multi-sensor data fusion architecture," *Applied Soft Computing*, vol. 69, pp. 149–164, 2018. [Online]. Available: <https://www.sciencedirect.com/science/article/pii/S1568494618302163>
- [18] M. K. Al-Sharman, Y. Zweiri, M. A. K. Jaradat, R. Al-Husari, D. Gan, and L. D. Seneviratne, "Deep-learning-based neural network training for state estimation enhancement: Application to attitude estimation," *IEEE Transactions on Instrumentation and Measurement*, vol. 69, no. 1, pp. 24–34, 2020.
- [19] M. Wabbah, M. Chehadeh, and Y. Zweiri, "Dynamic based estimator for uavs with real-time identification using dnn and the modified relay feedback test," 2021.
- [20] A. Ayyad, P. Silva, M. Chehadeh, M. Wabbah, O. AbdulHay, I. Boiko, and Y. Zweiri, *Multirotors From Takeoff to Real-Time Full Identification using MRFT and DNNs*, 2020. [Online]. Available: <https://youtu.be/NH58HskNqk4>
- [21] C. Cheron, A. Dennis, V. Semerjyan, and Y. Chen, "A multifunctional HIL testbed for multirotor VTOL UAV actuator," in *Proceedings of 2010 IEEE/ASME International Conference on Mechatronic and Embedded Systems and Applications*. IEEE, jul 2010, pp. 44–48. [Online]. Available: <http://ieeexplore.ieee.org/document/5552032/>
- [22] M. S. Chehadeh and I. Boiko, "Design of rules for in-flight non-parametric tuning of PID controllers for unmanned aerial vehicles," *Journal of the Franklin Institute*, vol. 356, no. 1, pp. 474–491, jan 2019. [Online]. Available: <https://linkinghub.elsevier.com/retrieve/pii/S0016003218306604>
- [23] D. Atherton, *Nonlinear Control Engineering: Describing Function Analysis and Design*. London: Van Nostrand Reinhold, 9 1975.
- [24] I. Boiko, "Modified relay feedback test (mrft) and tuning of pid controllers," in *Non-parametric Tuning of PID Controllers: A Modified Relay-Feedback-Test Approach*. London: Springer London, 2013, pp. 25–79. [Online]. Available: [https://doi.org/10.1007/978-1-4471-4465-6\\_3](https://doi.org/10.1007/978-1-4471-4465-6_3)
- [25] A. Rehan, I. Boiko, and Y. Zweiri, "Optimal non-parametric tuning of pid controllers based on classification of shapes of oscillations in modified relay feedback test," *Journal of the Franklin Institute*, vol. 358, no. 2, pp. 1448–1474, 2021.
- [26] K. Åström and T. Häggglund, "Automatic tuning of simple regulators with specifications on phase and amplitude margins," *Automatica*, vol. 20, no. 5, pp. 645–651, sep 1984. [Online]. Available: <https://www.sciencedirect.com/science/article/pii/0005109884900141>
- [27] R. Rohrer and M. Sobral, "Sensitivity considerations in optimal system design," *IEEE Transactions on Automatic Control*, vol. 10, no. 1, pp. 43–48, 1965.
- [28] O. AbdulHay, *Unified Identification and Tuning Approach Using DNN-MRFT For Visual Servoing Applications*, 2021. [Online]. Available: <https://youtu.be/G69OldaoIKQ>
- [29] B. Penin, P. R. Giordano, and F. Chaumette, "Vision-based reactive planning for aggressive target tracking while avoiding collisions and occlusions," *IEEE Robotics and Automation Letters*, vol. 3, no. 4, pp. 3725–3732, 2018.